

Investigating microstructure of Longmaxi shale in Shizhu area, Sichuan Basin, by optical microscopy, scanning electron microscopy and micro-computed tomography

Yu Wang^{1,2} · Li-Hua Wang^{1,2} · Jian-Qiang Wang^{1,2} · Zheng Jiang^{1,2} · Chan Jin^{1,2} · Yan-Fei Wang³

Received: 26 December 2016 / Revised: 1 June 2017 / Accepted: 11 June 2017 / Published online: 26 October 2017

© Shanghai Institute of Applied Physics, Chinese Academy of Sciences, Chinese Nuclear Society, Science Press China and Springer Nature Singapore Pte Ltd. 2017

Abstract Microstructure of shale formation is the key to understanding its petrophysical and chemical properties. Optical microscopy, scanning electron microscopy and micro-computed tomography (μ -CT) have been combined for characterization of microstructure of Longmaxi (LMX) shale from Shizhu area, Sichuan Basin. The results indicate that laminated LMX shale consists of mineral matrix-rich layers and organic matter (OM)-rich layers at micrometer scale in two and three dimensions. Mineral matrix layers, mainly consisting of interparticle pores and intraplatelet pores, are approximately parallel to the bedding plane. Pyrite-rich layer, mainly containing intercrystalline pores, shows a strong preferred orientation parallel to the bedding plane. OM-rich layer, mainly containing OM pores, seems to be discontinuous. In addition, intercrystalline pores are

enriched in some layers, while OM pores are distributed irregularly in matrix layers. This vertical heterogeneity of pore microscopic structures in LMX shale is of great importance to understand its petrophysical and chemical properties.

Keywords Micro-computed tomography · Pore microstructure · Heterogeneity · Matrix layers · Longmaxi shale

1 Introduction

Shale gas exploration has been in significant progresses in China in recent years, after its rapid and successful commercial development in North America [1–3]. Several horizons of organic-rich shale formations distributed in south China have garnered particular interest because of their high potential in exploration. Among these, the lower Palaeozoic of Sichuan Basin in southwestern China has been showing tremendous potential of shale gas development since the success in obtaining industrial gas flows in Weiyuan and Fuling areas. Chen [4] and Zhang et al. [5] reported that the Jiulaodong (JLD) shale in Weiyuan area and the Longmaxi (LMX) shale in Fuling area are characterized by large efficiency thickness, high thermal evolution degree, high brittle mineral content and suitable preservation condition. Geological researches indicate that the geochemical features of LMX shale in Shizhu area (in the middle of Sichuan Basin) are similar to those of the JLD shale in Weiyuan area and the LMX shale in Fuling area [6, 7], suggesting a favorable horizon for shale gas exploration and development.

This work was supported by the Strategic Priority Research Program of the Chinese Academy of Sciences (No. XDB1002010), the Major Program for the Fundamental Research of Shanghai Committee of Science and Technology (No. 12JC1410400) and the National Natural Science Foundation of China for Distinguished Young Scholars (No. 41325016).

✉ Li-Hua Wang
lhwang@sinap.ac.cn

Yu Wang
yuwang@sinap.ac.cn

- ¹ Key Laboratory of Interfacial Physics and Technology, Shanghai Institute of Applied Physics, Chinese Academy of Sciences, Shanghai 201800, China
- ² Shanghai Synchrotron Radiation Facility, Shanghai Institute of Applied Physics, Chinese Academy of Sciences, Shanghai 201204, China
- ³ Institute of Geology and Geophysics, Chinese Academy of Sciences, Beijing 100029, China

Microscopic pore structure, which is significant for shale gas storing status and migration pattern, has been a focus of shale gas research [8–10]. Shale gas development in North America has made great progress since scanning electron microscope (SEM) coupled with Ar-ion milling technique was adopted for pore characterization by Loucks et al. [11]. Nanometer-to-micrometer pores in shale have been found worldwide using Ar-ion milling and SEM technique, and different kinds of pore classifications have been proposed [11–14]. These pores are generally classified into three types according to their relationships to minerals, namely interparticle pores, intraparticle pores and OM pores. Intraparticle pores are further divided into intraplatelet pores within clay aggregates, intercrystalline pores within pyrite, dissolved pores, moldic pores after fossils, etc. [12]. Pore structures are characterized based on the differences in origin, size, shape and connectivity, which may lead to varied contributions to gas storage and permeability. Each mineral phase often has its own pore structures [15–17]. SEM investigations also show that even the same formation from an area has different pore structures at the scales from micrometer to centimeter [18, 19]. Understanding these heterogeneities of pore structures in shale is of great importance to reserve assessment and effective hydraulic fracturing designation.

SEM mainly provides images of pore structures in two dimensions, but 3D morphology is needed. Focused ion beam scanning electron microscopy (FIB-SEM) and X-ray computed tomography (X-CT) are main methods used to investigate pore structures of shale in three dimensions [20–22]. FIB-SEM is usually capable of providing successive micrographs down to several nanometers which can be stacked to rebuild the microstructures of pores and minerals in three dimensions. However, FIB-SEM brings unrecoverable destruction to the sample, making it impossible for further studies with other methods [20, 23]. Compared to FIB-SEM, X-ray computed tomography (X-CT) is a non-destructive method capable of observing pore structures and networks from micrometers down to several hundreds of nanometers [21, 22, 24]. As the X-ray absorption coefficients of pores and minerals are different, it is possible to distinguish them and reconstruct the model of each phase in three dimensions.

In this paper, microstructures of LMX shale from Shizhu area are investigated by optical microscope, SEM and μ -CT with resolution down to 1.625 μm . The primary purpose is to assess the heterogeneity of minerals and organic matters in LMX shale. It is expected that petrophysical and chemical properties of LMX shale could be better understood.

2 Samples and experiments

2.1 Geological background and sample

Shizhu area is located in Chongqing Province in the middle Sichuan Basin of Western Hubei fold belt of central upper Yangtze platform (Fig. 1a) [25]. The gas accumulation occurred successively during the Indosinian Movement and Himalaya Movement. Cambrian, Ordovician, Silurian, Carboniferous and Triassic strata exposed have been confirmed favorable horizons for shale gas accumulation.

The LMX shale samples were collected in Dafengao outcrop, Shizhu area. The LMX shale, which is the natural extension from Pengshui area to Qiliao areas, is a stable suite of marine clastic deposition consisting of black carbonous shale of 3–4 m in thickness together with pyrite and quartz veins [26]. The strike of LMX shale is N35°E with a dipping angle of 62° (Fig. 1b, c). Total organic carbon (TOC) contents of LMX sample are 2.92%, and X-ray diffraction analysis shows that it contains quartz (50%), plagioclase (15%), calcite (5%), dolomite (4%), pyrite (4%), illite (14%), illite-smectite mixed layer (6%) and chlorite (2%).

2.2 Methods

For optical microscopy, thin-section samples perpendicular to bedding were prepared by cutting the drill samples and impregnating about 7–8 mm long with epoxy and polishing them down to a thickness about 30 μm after hardening. They were with a Zeiss HAL100 optical microscope using magnification of 10 \times under cross-polarized light.

Samples for SEM were prepared by ion milling technique using LJB 1A with an accelerating voltage of 5 kV and a gun current of 100 μA for 10–12 h [14]. The 2D microstructures were imaged with a Zeiss Merlin Compact LE0 1530 VP equipped with EDS (energy-dispersive spectroscopy, Oxford Instruments), at acceleration voltage of 5 kV with working distance of 5–6 mm and 15 kV and 8–10 mm for EDS analysis to identify the minerals.

Shale samples for μ -CT were ground manually with sandpaper into small cylinders ($\sim \Phi 3 \text{ mm} \times 6 \text{ mm}$). The μ -CT experiments were carried out on beamline BL13W1 at Shanghai Synchrotron Radiation Facility (SSRF), which was operated at 3.5 GeV and 230 mA in top-up mode. The BL13W1 is illustrated in Fig. 2. X-rays are generated in a 16-pole wiggler with magnetic field of 1.9 T and magnetic period length of 14 cm. The white beam is monochromatized by a Si(111) double-crystal monochromator. The X-ray photons of selected energy passing through a sample

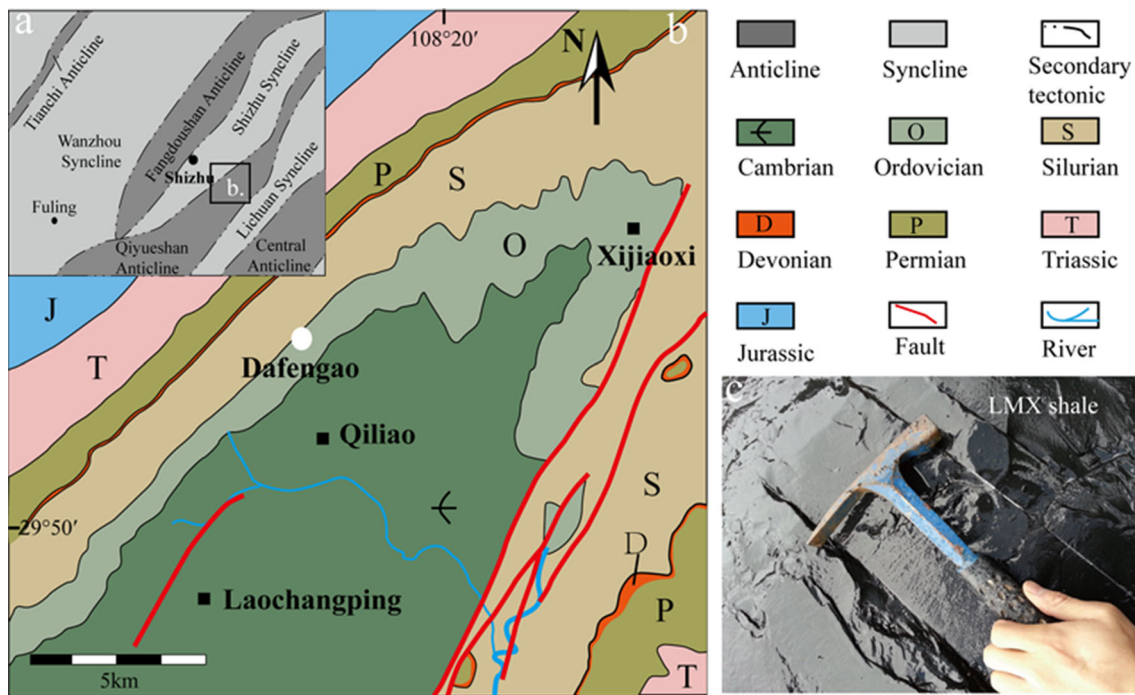


Fig. 1 (Color online) Tectonic and geological maps (a, b) of Dafengao and its neighboring areas in Sichuan Basin, eastern Chongqing Province, China (simplified Refs. [25, 26]) and the LMX shale at Dafengao outcrop (c)

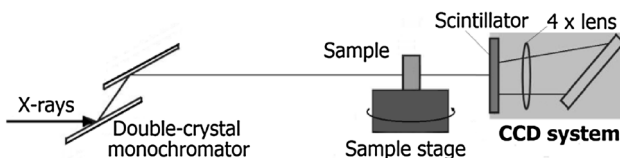


Fig. 2 Schematic diagram of BL13W1 in Shanghai synchrotron radiation facility

rotating on its vertical axis are received by the CCD system with a scintillator [27]. In the experiments, the X-ray energy was 25 keV, the sample-CCD distance was 10 cm, the sample was mounted on the stage rotated in 0.167° steps for a total of 180° , the exposure time for each view was 2.5 s, and 1080 projection images were acquired for each sample. Dark current of the detector system was measured after the CT measurement for correction.

Image reconstruction was performed using PITRE (Phase-sensitive X-ray image processing and tomography reconstruction) software in-house developed for the beamline [28]. Firstly, five dark-field images and 38 bright-field images were used to correct intensity modulations, so as to remove artifacts in the slice to be reconstructed. Next, the tomography data were transformed into the sinogram, which represented the signal of a given detector row in the imaging plane for all projection angles. Then, the sinogram was normalized in case to provide sufficiently homogeneous intensity variations during data acquisition. Finally, the data were reconstructed based on the filtered back-

projection algorithm [29] and exhibited in 32-bit TIF format, which were transformed into 8-bit TIF format using integer numbers to represent grayscale values of 2^8 shades in the shale sample.

3D tomographical data were analyzed using Avizo Fire Software 8.0. Sub-volume of $1950 \mu\text{m} \times 1300 \mu\text{m} \times 2275 \mu\text{m}$ was extracted and smoothed with a non-local means filter. Local thresholding schemes based on the indicator kriging method [30] were adopted for image segmentation. Gray histograms related to different X-ray absorption coefficients of different phases were used to segment the low-density matter (pores and OM) and the mineral matrix. The threshold value interval of low-density matter and mineral was manually selected by visual inspection. With the above segmentations, the 3D structural information of the Longmaxi shale sample was reconstructed and visualized.

3 Results and discussion

3.1 Optical microscopy

Optical microscopy in Fig. 3a shows good layered structures of the LMX shale. Main components such as inorganic mineral matrix-rich layers (brown) and organic matter-rich layers (black) heterogeneously distribute on submillimeter scale. The OM-rich layers are interbedded

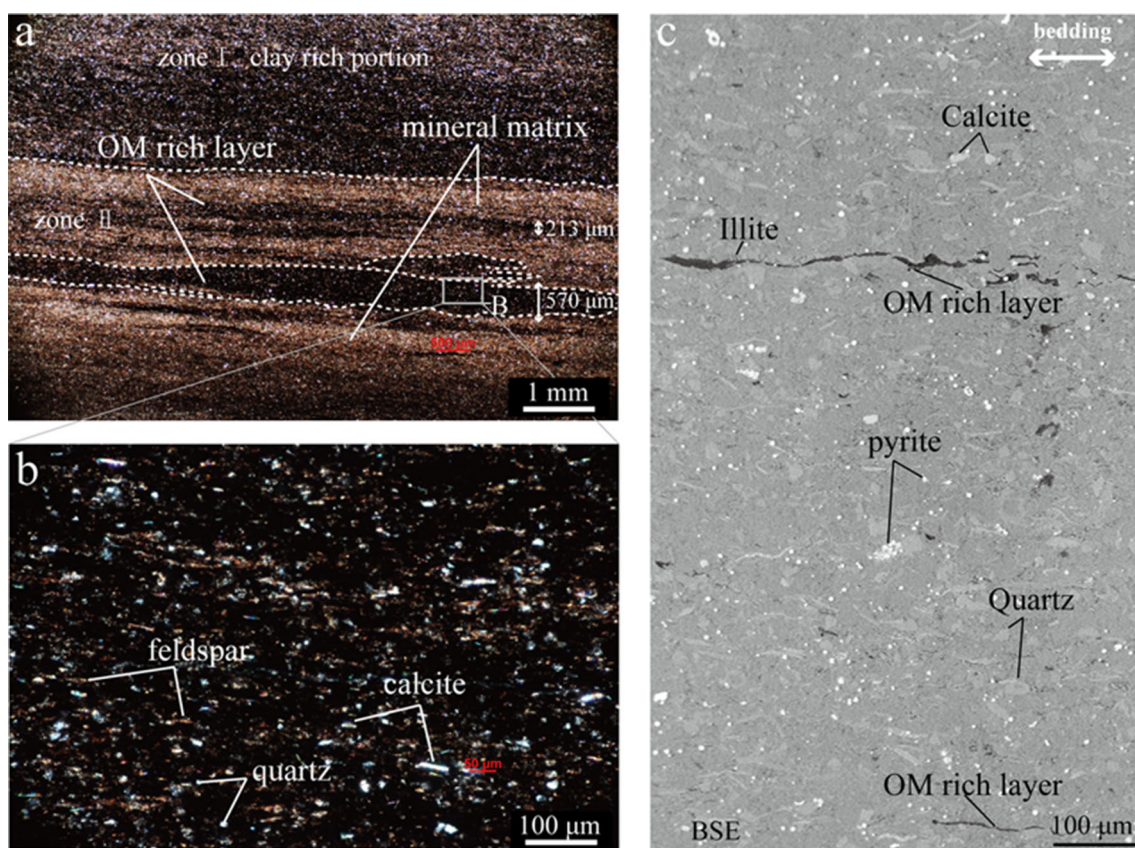


Fig. 3 (Color online) Microscopic characteristics of the LMX shale. **a** Thin section showing mineral-rich layer and organic-rich layer. The dashed line shows the boundary between mineral matrix-rich layer and OM-rich layer. **b** Close-up micrograph of the rectangular portion

in **a**, where quartz, calcite and alternating feldspars scatter in the OM and clay matrix. **c** SEM image showing layered structures and main mineral phases in LMX shale

irregularly in inorganic mineral matrix-rich layers, with an average content of about 10%. The mineral matrix-rich layers are in width of hundreds of micrometers to several millimeters, orientating approximately parallel to the bedding plane, while the OM layers are in hundred micrometers, wedge-shaped and discontinuous.

The mineral matrix layers consist of mainly quartz, calcite and feldspars (Fig. 3b). Quartz (white) is characterized by fine grain and well psephicity. The crystal form of feldspar (bright brown) is barely visible. Calcite identified by pleochroism is elongated and exhibits weak orientation.

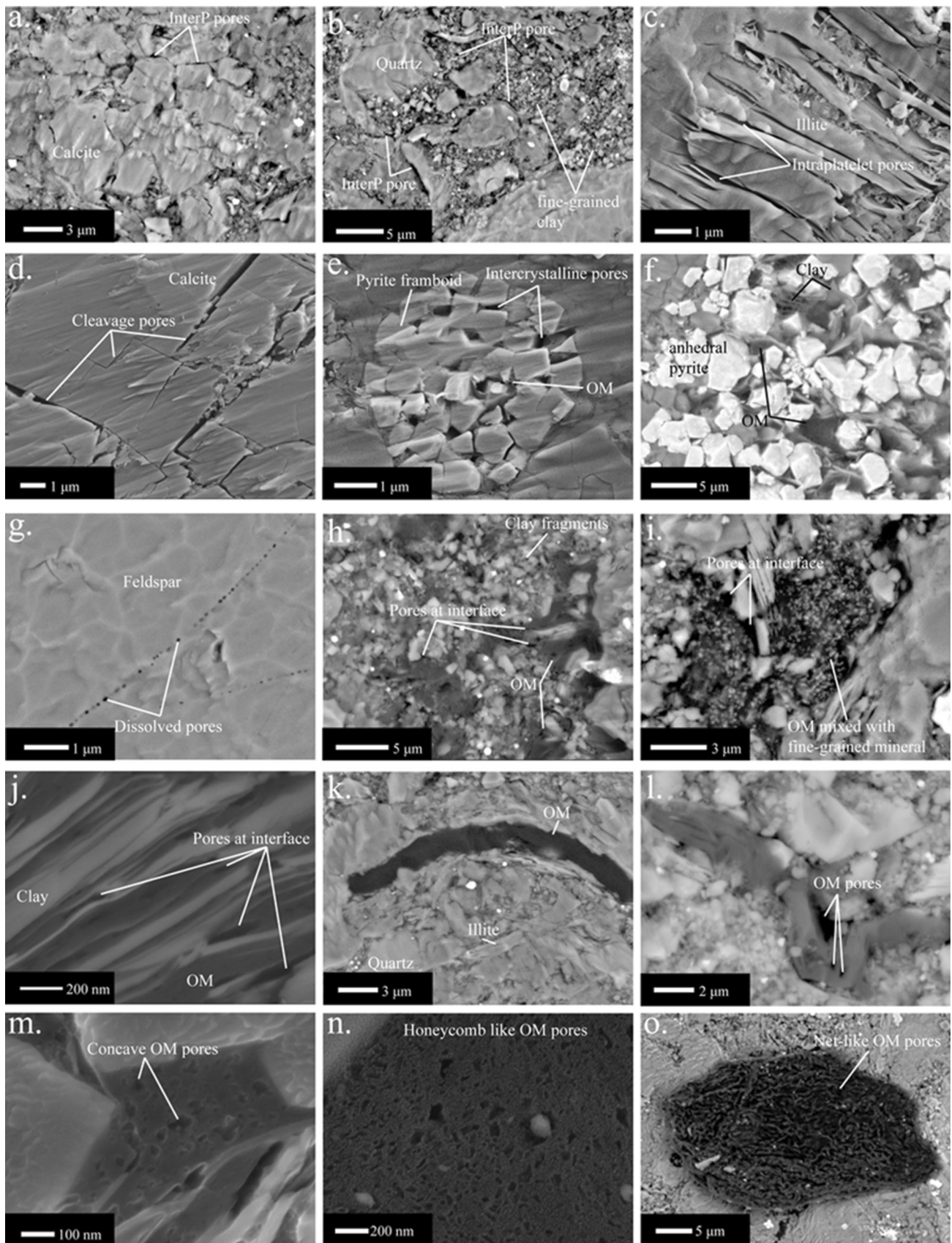
3.2 SEM analysis

SEM observations show that minerals and organic matter were embedded in the clay matrix. Minerals are distributed homogeneously at submillimeter scale, and organic matter exhibits weak oblique bedding with elongated wedge shape and discontinuous distribution. Non-porous and porous OMs, and phases of quartz, feldspar,

calcite, dolomite, pyrite and illite, can be identified based on EDS analysis results.

As shown in Fig. 4a–g, the main pore types contained the minerals are interparticle pores, intraparticle pores, intercrystalline pores, dissolved pores and cleavage pores. The interparticle pores mainly developed around or between mineral fragments as quartz, feldspar and calcite are of rectangle, triangle or narrow shapes sized from hundreds of nanometers to a few micrometers. Figure 4a shows calcite with narrow interparticle pores between fragments. Figure 4b shows quartz fragments scattering in

Fig. 4 SEM images of the LMX shale. **a** Interparticle pores between calcite fragments. **b** Interparticle pores at the interface. **c** Intraplatelet pores within clay aggregates. **d** Cleavage pores. **e** Intercrystalline pores within pyrite framboids. **f** Intercrystalline pores within anhedral pyrite. **g** Dissolved pores in feldspar. **h** OM scatters in clay mineral fragments. **i** OM mixed with fine-grained minerals. **j** Non-porous OM occupied intraplatelet pores with narrow pores at interface. **k** Arc-shaped non-porous OM. **l** OM pores related to clay minerals. **m** Cavernous OM pores. **n** Honeycomb-like OM pore. **o** Network like OM pore



fine-grained clay mineral clasts, forming narrow interparticle pores at the interface. Plenty of irregular interparticle pores sized at hundreds of nanometers are found in the fine-grained clay mineral clasts. Figure 4c illustrates that intraparticle pores with sheet-like and elongated shape are observed in laminar illite. These intraparticle pores are generally a few micrometers long, in parallel orientation to illite, indicating a good connectivity in this direction. Figure 4d illustrates narrow cleavage pores forming along mechanic weak plane in calcite. In Fig. 4e, the intracrystalline pores are of typical framboid pyrite. In Fig. 4f, some pyrites exhibit as anhedral existing together with clay sheet and porous OM. Most intercrystalline pores are triangular or rectangular sized at hundreds of nanometers. The pyrite pores show a poor connectivity due to their OM contents. Round pores of Φ 100–300 nm are dissolved pores in feldspar (Fig. 4g).

Non-porous and porous OMs are shown in Fig. 4h–o. This refers to the tight matter without pores and internal structure, scattered usually in the mineral matrix pores, sized from a few to tens of micrometers, in irregular or band shapes depending on the shape of mineral matrix pores. In Fig. 4h, irregular OM particles in dark gray color are dispersive in clay mineral clasts. OM is also intimately mixed with fine-grained minerals (Fig. 4i). In Fig. 4j, relatively dark OM in band shape can be seen between intraplatelet pores within clay aggregates, and a few narrow pores exist at the interface between this kind of OM and mineral grains. Figure 4k shows arc-shaped OM, embedded in clay clasts. It seems that this type of OM is less contacted with mineral phases, but a few small pores can be identified within it.

Porous OM is characterized by OM pores of different shapes and sizes. OM absorbed to the clay surface forms narrow pores (Fig. 4l). Their shapes are likely determined by clay mineral orientation, indicating that clay minerals are significant for catalytic models of organic hydrocarbon generation mechanisms. Most of the porous OM particles contain cavernous or honeycomb OM pores sized from several tens to over a hundred nanometers. The shape of this type OM pores is round or concave (Fig. 4m, n). Finally, Fig. 4o shows well-developed network-like OM pores, with good interconnectivity.

3.3 Micro-computed tomography

With different X-ray absorption efficiency, different grayscale values can be obtained in 2D reconstructed slices. Figure 5a, b shows typical gray values along the dashed line. For areas are investigated. The highest absorbing areas (bright) are identified as pyrite, while the intermediate shades is a mixture of quartz, feldspar, calcite and clay minerals (Fig. 5c, d). The lowest absorbing areas

are low-density matter (dark gray color), containing OM and pores. It is an impossible task to determine accurate threshold values because the gray level distribution in shale is continuous, lacking clearly peaks or valleys in the gray value histogram. The closeness of absorption efficiencies of OM and pore is another factor hindering their segmentation due to the limitation of human vision. In this paper, low-density matter is identified as OM considering the following two reasons. Firstly, along one line indicating the grayscale threshold of low-absorbing features, the gray values of around 70–80 (barely dark) represent OM. Secondly, SEM observations indicate that pores are characterized by rectangle, triangle, sheet-like, round or narrow shapes sized from tens of nanometers to a few micrometers. On the contrary, low-density matter mapped by μ -CT is mainly wedge-shaped and discontinuous in bedding direction, sized from a few to dozens of micrometers. Inferred from the distribution and morphology together with SEM images, the irregular discrete low-density matter scatter in mineral matrix is identified as OM.

Figure 5e shows the reconstructed LMX shale microstructure of $1300 \mu\text{m} \times 1950 \mu\text{m} \times 2275 \mu\text{m}$, with the X – Y plane being parallel to the bedding plane. In the left, OM-rich layer and pyrite-rich layer of a submillimeter can be seen clearly along the Z -axis. Mineral matrix layer, especially pyrite-rich layer, shows a strong preferred orientation parallel to the bedding plane (in the X – Y plane). OM-rich layers scatter in mineral matrix unevenly. The right part of Fig. 5e is 3D visualization of organic matter and pyrite without other types of mineral matrix.

Figure 6a shows the reconstructed 3D visualizations of OM. Smaller OMs ($< 0.75 \text{ mm}^3$) scatter mainly in mineral matrix throughout the LMX shale sample. The larger ones ($> 0.75 \text{ mm}^3$) are wedge-shaped and intersected roughly with the bedding plane at small angles. The volume ratio of OM decided by CT is 1.8%, suggesting a low content of organic carbon. Generally, OM is heterogeneously distributed, including a few concentrations in some bedding planes, as shown in Fig. 6a, b. In Fig. 6b, the OM volume fraction graph suggests that the bedding planes corresponding to Slices 42, 167, 264 and 980 may contain more OM. The heterogeneity is further illustrated in Fig. 6c from a series of micrographs taken perpendicular to the bedding. The micrographs from left to right successively corresponded to reconstructed Slices 1, 100, 200, 300, 400 and 900 in Y – Z plane along X -axis. In Fig. 6c, larger OM particle in Slice 1 can be seen clearly and completely in Slice 100 but not in Slice 300, and can hardly be seen in Slice 400. Meanwhile, new OM particles in other bedding planes appear gradually as shown in Slices 400 and 900. The size and morphology of OM are consistent with SEM results, indicating a vertical heterogeneous distribution and discontinuity.

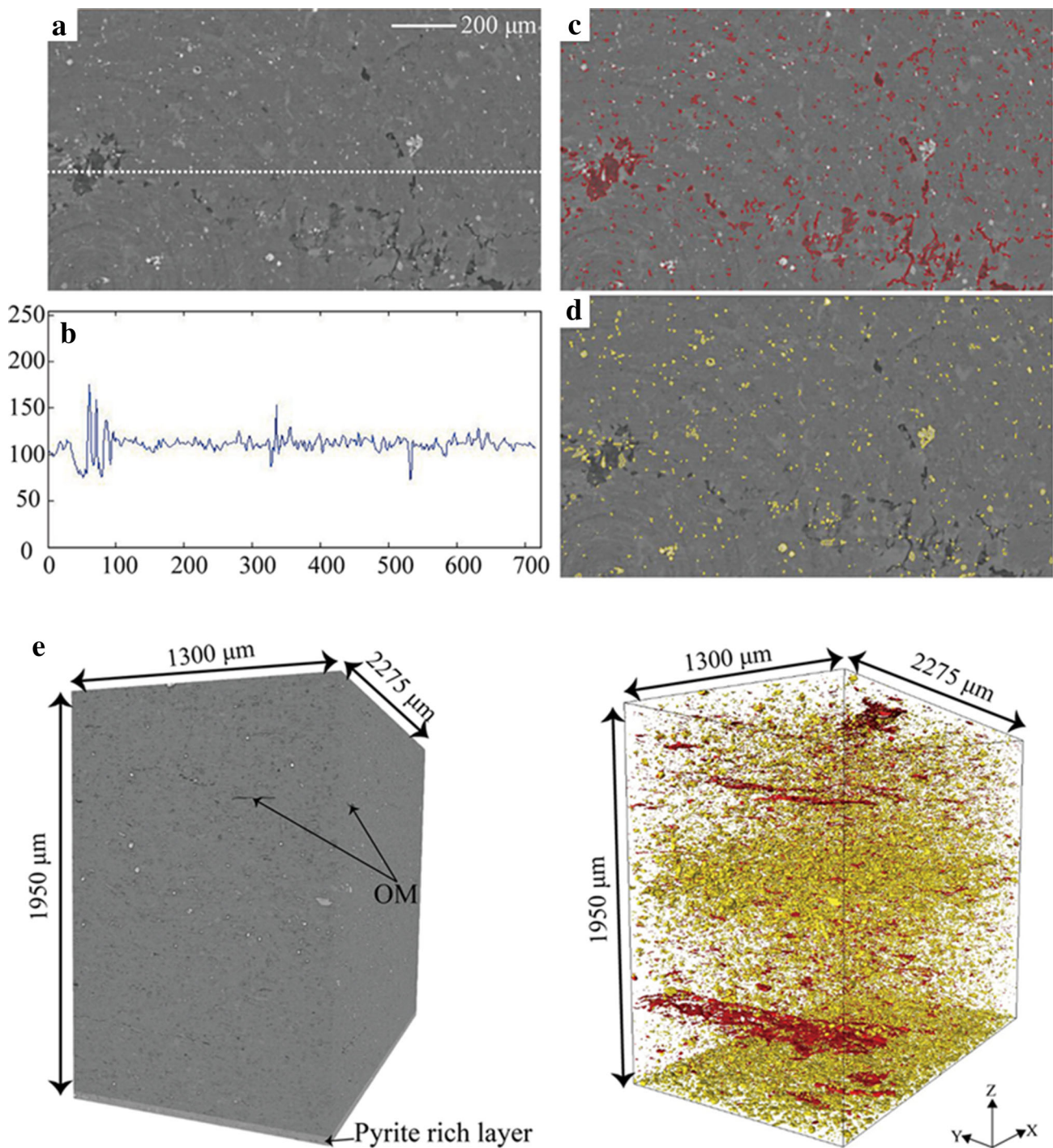


Fig. 5 (Color online) Images in the X - Y plane of Longmaxi black shale. **a** Reconstructed slice after applying non-local means filter. **b** The values plotted gray along dash line in **a** suggest organic matter and pyrite clearly. **c** Thresholding boundary of organic matter.

d Thresholding boundary of pyrite. **e** Reconstructed 3D microstructure of LMX shale at millimeter scale and 3D visualization of organic matter (red) and pyrite (yellow)

Figure 6d shows 3D visualization of pyrite. The volume ratio of pyrites decided by CT is 11.6%, being consistent with the SEM result. Pyrites are mainly organized into framboids and disperse heterogeneously throughout LMX shale sample. Compared with OM, most pyrites are

relatively ordered and continuous with preferred orientation along the bedding plane, indicating the development of pyrite veins on the micrometer scale (Fig. 6d). The two peaks in pyrite volume fraction graph represent the pyrite-rich portion. The first peak, corresponding to Slice 400–700

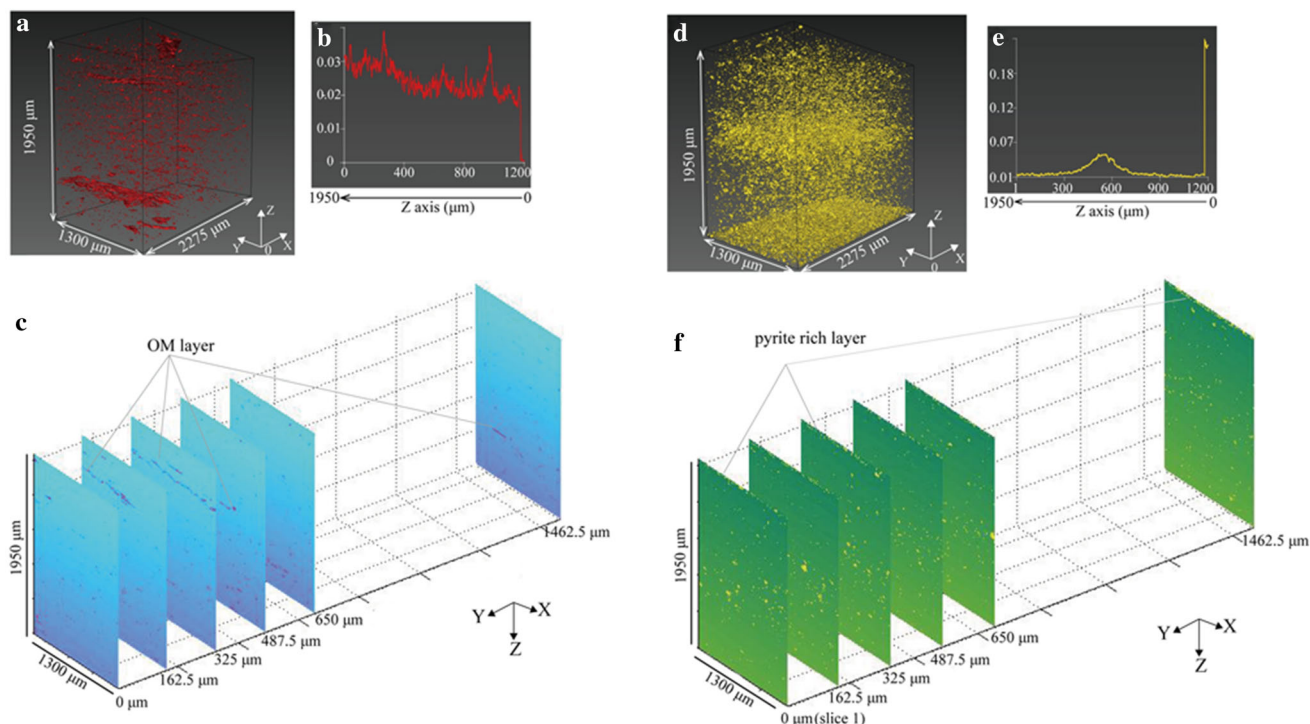


Fig. 6 (Color online) **a** 3D visualization of OM. **b** Volume fraction plotting along Z direction, reflecting a small variation of OM contents in different bedding planes. **c** Micrographs taken perpendicular to the bedding indicate OM is heterogeneously distributed and discontinuous in 3D. **d** 3D visualization of pyrite. **e** Volume fraction plotting

(488 μm thick), is wide and gentle (Fig. 6e), while the second peak is sharp and much higher, indicating that the whole layer is almost occupied by pyrites probably due to abundant source of Fe^{2+} in the sedimentary environment at that time. Figure 6f shows micrographs taken perpendicular to the bedding. From left to right successively corresponded to reconstructed Slices 1, 100, 200, 300, 400 and 900 in Y–Z plane along X-axis. The pyrite-rich layers viewed in Slice 100 can be seen in other slices, indicating a good extensity in the bedding plane. Both SEM observations and 3D visualization confirmed that pyrite distributes heterogeneously and enriched in some layers along the vertical direction.

3.4 Significance for shale gas storage and transportation

As the origin of OM pores, OM has a positive influence on shale gas occurrence. OM pores not only offer the main storage space for absorbed shale gas, but also form the dominant or subsidiary pore network in shale gas-oil transportation system [12]. The final connectivity of OM pore network depends on the OM distribution [31]. For high maturity shale samples dominated by OM-hosted porosity, the development of OM pores is related to both

along Z direction, reflecting a large variation of pyrite contents in different bedding planes. **f** Micrographs taken perpendicular to the bedding indicates pyrite are heterogeneously distributed and relatively continuous in 3D

OM and mineral. SEM observations indicate that OM pores preserved in LMX shale sample consist of pores within OM or between OM, sized from tens of nanometers to a few micrometers. The widely developed nanometer scale OM pores are significant for absorbed shale gas storage. The results of $\mu\text{-CT}$ indicate that the OM in LMX shale sample distributes heterogeneously perpendicular to the bedding plane. Therefore, the porosity and connectivity can be improved with increased thermal maturity due to the good continuity of OM, especially in the bedding.

The 3D distribution characteristics of pyrite indicate that intercrystalline pores are also enriched in some layers along the vertical direction, showing heterogeneity perpendicular to the bedding plane. This suggests that main pore types in LMX shale samples may differ from one layer to another at the micrometer scale. Since the number and size of different types of pores vary from each other, the porosity of different matrix layers is also diverse. The conclusion is helpful for building physical and mathematical models of the matrix porosity for shale rocks. From preliminary studies on LMX shale from south Sichuan area, Wang et al. [32] built a rock physical model of brittle mineral, clay mineral and OM layers and proposed a formula for porosity estimation, as expressed by

$$\rho A_{\text{Bri}} V_{\text{Bri}} + \rho A_{\text{Clay}} V_{\text{Clay}} + \rho A_{\text{TOC}} V_{\text{TOC}} = \varphi \quad (1)$$

where ρ is rock density (t/m^3), A is mineral percent content, V is pore volume per unit mass (m^3/t), and φ is defined as shale porosity. The formula has been confirmed efficient in shale porosity quantification.

4 Conclusion

Optical microscopy, scanning electron microscopy and micro-computed tomography have been combined in characterizing the microstructure of Longmaxi shale from Shizhu area, Sichuan Basin. The results indicate that the laminated LMX shale consists of mineral matrix-rich layers and organic matter-rich layers at micrometer scale. The mineral matrix layers, mainly consisting of interparticle pores and intraplatelet pores, are approximately parallel to the bedding plane. The pyrite-rich layer, mainly containing intercrystalline pores, shows a strong preferred orientation parallel to the bedding plane. The OM-rich layer, mainly containing OM pores, is irregularly shaped and discontinuously distributed. The intercrystalline pores are enriched in some layers, while OM pores are distributed irregularly in matrix layers. This vertical heterogeneity of microscopic structures of pores in LMX shale is crucial to its petrophysical and chemical properties.

Acknowledgements The authors would thank staff at beamline BL13W of Shanghai Synchrotron Radiation Facility (SSRF) for their kind help with μ -CT experiment. We also thank Prof. Guang-Jun Guo and Dr. Ming Geng from Institute of Geology and Geophysics, Chinese Academy of Sciences, for providing geological background and field sampling.

References

1. Y.M. Li, G.H. Liu, J. Li et al., Improving fracture initiation predictions of a horizontal wellbore in laminated anisotropy shales. *J. Nat. Gas Sci. Eng.* **24**, 390–399 (2015). doi:10.1016/j.jngse.2015.04.002
2. Y. Wan, Z.J. Pan, S.H. Tang et al., An experimental investigation of diffusivity and porosity anisotropy of a Chinese gas shale. *J. Nat. Gas Sci. Eng.* **23**, 70–79 (2015). doi:10.1016/j.jngse.2015.01.024
3. J. Xiong, X.J. Liu, L.X. Li, Experimental study on the pore structure characteristics of the Upper Ordovician Wufeng Formation shale in the southwest portion of the Sichuan Basin, China. *J. Nat. Gas Sci. Eng.* **22**, 530–539 (2015). doi:10.1016/j.jngse.2015.01.004
4. Z.Q. Chen, Shale gas exploration in Jiulaodong formation of lower Cambrian Sichuan Basin. *China Pet. Explor.* **5**, 71–78 (2012). doi:10.3969/j.issn.1672-7703.2012.05.011 (in Chinese)
5. S.W. Zhang, Z.Y. Meng, Z.F. Guo et al., Characteristics and major controlling factors of shale reservoirs in the Longmaxi Fm, Fuling area Sichuan Basin. *Nat. Gas Ind.* **34**(12), 16–24 (2014). doi:10.3787/j.issn.1000-0976.2014.12.002 (in Chinese)
6. C.N. Zou, J.H. Du, C.C. Xu et al., Formation, distribution, resource potential, and discovery of Sinian–Cambrian giant gas field, Sichuan Basin SW China. *Pet. Explor. Dev.* **41**(3), 306–325 (2014). doi:10.1016/S1876-3804(14)60036-7
7. C.N. Zou, G.Q. Wei, C.C. Xu et al., Geochemistry of the Sinian–Cambrian gas system in the Sichuan Basin China. *Org. Geochem.* **74**, 13–21 (2014). doi:10.1016/j.orggeochem.2014.03.004
8. C.R. Clarkson, N. Solano, R.M. Bustin et al., Pore structure characterization of North American shale gas reservoirs using USANS/SANS, gas adsorption, and mercury intrusion. *Fuel* **103**, 606–616 (2013). doi:10.1016/j.fuel.2012.06.119
9. M. Pommer, K. Milliken, Pore types and pore-size distributions across thermal maturity, Eagle ford formation, southern Texas. *AAPG Bull.* **99**(09), 1713–1744 (2015). doi:10.1306/03051514151
10. L. Ma, K.G. Taylor, P.D. Lee et al., Novel 3D centimetre-to nano-scale quantification of an organic-rich mudstone: the Carboniferous Bowland Shale Northern England. *Mar. Pet. Geol.* **72**, 193–205 (2016). doi:10.1016/j.marpetgeo.2016.02.008
11. R.G. Loucks, R.M. Reed, S.C. Ruppel et al., Morphology, genesis and distribution of nanometer-scale pores in siliceous mudstones of the Mississippian Barnett shale. *J. Sediment. Res.* **79**(12), 848–861 (2009). doi:10.2110/jsr.2009.092
12. R.G. Loucks, R.M. Reed, S.C. Ruppel et al., Spectrum of pore types and networks in mudrocks and a descriptive classification for matrix-related mudrock pores. *AAPG Bull.* **96**(6), 1071–1098 (2012). doi:10.1306/08171111061
13. C.N. Zou, R.K. Zhu, B. Bai et al., First discovery of nano-pore throat in oil and gas reservoir in China and its scientific value. *Acta Petrol. Sin.* **27**(6), 1857–1864 (2011). doi:1000-0569/2011/027(06)-1857-64 (in Chinese)
14. Y. Wang, C. Jin, L.H. Wang et al., Characterization of pore structures of Jiulaodong formation shale in the Sichuan Basin by SEM with Ar-ion milling. *Rock Miner. Anal.* **34**(3), 278–285 (2015). doi:10.15898/j.cnki.11-2131/td.2015.03.003 (in Chinese)
15. Q.R. Passey, K.M. Bohacs, W.L. Esch et al., From oil-prone rock to gas-producing shale reservoir—geological and petrophysical characterization of unconventional shale-gas reservoirs. in *International Oil and Gas Conference and Exhibition in China*. Society of Petroleum Engineers, Beijing, China (2010) p. 29. SPE 131350
16. J. Klaver, G. Desbois, R. Littke et al., BIB-SEM characterization of pore space morphology and distribution in postmature to overmature samples from the Haynesville and Bossier Shales. *Mar. Pet. Geol.* **59**, 451–466 (2015). doi:10.1016/j.marpetgeo.2014.09.020
17. K.E. Washburn, J.E. Birdwell, M. Foster et al., Detailed description of oil shale organic and mineralogical heterogeneity via Fourier transform infrared microscopy. *Energy Fuels* **29**(7), 4264–4271 (2015). doi:10.1021/acs.energyfuels.5b00807
18. Y.Y. Chen, M. Mastalerz, A. Schimmelmann, Heterogeneity of shale documented by micro-FTIR and image analysis. *J. Microsc.* **256**(3), 177–189 (2014). doi:10.1111/jmi.12169
19. X.Z. Wang, L.X. Zhang, C. Gao, The heterogeneity of Lacustrine shale gas reservoir in Yanchang Formation, Xiasiwan Area Ordos Basin. *Acta Geol. Sin.* **89**, 99–101 (2015). doi:10.1111/1755-6724.12302_42
20. J.E. Heath, T.A. Dewers, B.J.O.L. McPherson et al., Pore networks in continental and marine mudstones: characteristics and controls on sealing behavior. *Geosphere* **7**(2), 429–454 (2011). doi:10.1130/GES00619.1
21. W. Kanitpanyacharoen, D.Y. Parkinson, F. DeCarlo et al., A comparative study of X-ray tomographic microscopy on shales at different synchrotron facilities: ALS APS and SLS. *J. Synchrotron Radiat.* **20**(Pt 1), 172–180 (2013). doi:10.1107/S0909049512044354

22. B. Bai, R.K. Zhu, S.T. Wu et al., Multi-scale method of Nano(Micro)-CT study on microscopic pore structure of tight sandstone of Yanchang Formation Ordos Basin. *Pet. Explor. Dev.* **40**(3), 354–358 (2013). doi:[10.1016/S1876-3804\(13\)60042-7](https://doi.org/10.1016/S1876-3804(13)60042-7)
23. M.E. Curtis, C.H. Sondergeld, R.J. Ambrose et al., Microstructural investigation of gas shales in two and three dimensions using nanometer-scale resolution imaging. *AAPG Bull.* **96**(4), 665–677 (2012). doi:[10.1306/08151110188](https://doi.org/10.1306/08151110188)
24. P. Zhang, J.Q. Li, L.J. Xie et al., The quantitative characterization of heterogeneity using nanometer CT technique on the shale reservoir. *Acta Geol. Sin.* **89**, 134–135 (2015). doi:[10.1111/1755-6724.12302_56](https://doi.org/10.1111/1755-6724.12302_56)
25. Y.G. Hou, S. He, J.Z. Yi et al., Effect of pore structure on methane sorption capacity of shales. *Pet. Explor. Dev.* **41**(2), 248–256 (2014). doi:[10.11698/PED.2014.02.17](https://doi.org/10.11698/PED.2014.02.17) (in Chinese)
26. Y. Wang, C. Jin, Z. Jiang et al., Mineral composition and microscopic pore characteristics of Wufeng–Longmaxi Formation Shale in Eastern Chongqing City China. *Acta Mineralogica Sin.* **36**(04), 555–562 (2016). doi:[10.16461/j.cnki.1000-4734.2016.04.016](https://doi.org/10.16461/j.cnki.1000-4734.2016.04.016) (in Chinese)
27. H.L. Xie, B. Deng, G.H. Du et al., Latest advances of X-ray imaging and biomedical applications beamline at SSRF. *Nucl. Sci. Tech.* **26**(020102), 1–16 (2015). doi:[10.13538/j.1001-8042/nst.26.020102](https://doi.org/10.13538/j.1001-8042/nst.26.020102)
28. R.C. Chen, D. Dreossi, L. Mancini et al., PITRE: software for phase-sensitive X-ray image processing and tomography reconstruction. *J. Synchrotron Radiat.* **19**(Pt 5), 836–845 (2012). doi:[10.1107/S0909049512029731](https://doi.org/10.1107/S0909049512029731)
29. A.C. Kak, M. Slaney, G. Wang, Principles of computerized tomographic Imaging. *Med. Phys.* **29**(1), 107–114 (2002). doi:[10.1118/1.1455742](https://doi.org/10.1118/1.1455742)
30. W. Oh, W.B. Lindquist, Image thresholding by Indicator Kriging. *IEEE Trans. Pattern Anal.* **21**(7), 590–602 (1999). doi:[10.1109/34.777370](https://doi.org/10.1109/34.777370)
31. R.G. Loucks, R.M. Reed, Scanning-electron-microscope petrographic evidence for distinguishing organic matter pores associated with depositional organic matter versus migrated organic matter in mudrocks. *Gulf Coast Assoc. Geo Soc. J.* **3**, 51–60 (2014)
32. D.F. Wang, Y.M. Wang, D.Z. Dong et al., Quantitative characterization of reservoir space in the Lower Cambrian Qiongzhusi shale Southern Sichuan Basin. *Nat. Gas Ind.* **33**(7), 1–10 (2013). doi:[10.3787/j.issn.1000-0976.2013.07.001](https://doi.org/10.3787/j.issn.1000-0976.2013.07.001) (in Chinese)